

TransCMD: Cross-Modal Decoder Equipped with Transformer for RGB-D Salient Object Detection

Youwei Pang, Xiaoqi Zhao, Lihe Zhang, and Huchuan Lu

Abstract—Most of the existing RGB-D salient object detection methods utilize the convolution operation and construct complex interweave fusion structures to achieve cross-modal information integration. The inherent local connectivity of convolution operation constrains the performance of the convolution-based methods to a ceiling. In this work, we rethink this task from the perspective of global information alignment and transformation. Specifically, the proposed method (TransCMD) cascades several cross-modal integration units to construct a top-down transformer-based information propagation path (TIPP). TransCMD treats the multi-scale and multi-modal feature integration as a sequence-to-sequence context propagation and update process built on the transformer. Besides, considering the quadratic complexity w.r.t. the number of input tokens, we design a patch-wise token re-embedding strategy (PTRE) with acceptable computational cost. Experimental results on seven RGB-D SOD benchmark datasets demonstrate that a simple two-stream encoder-decoder framework can surpass the state-of-the-art purely CNN-based methods when it is equipped with the TIPP.

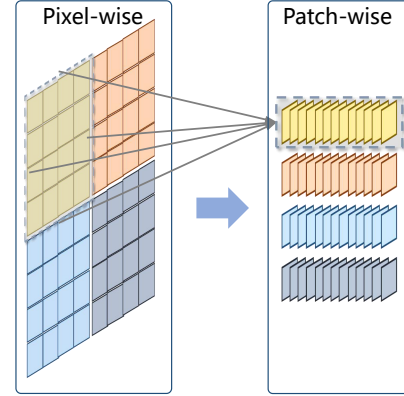


Fig. 1. Patch-wise token re-embedding (PTRE). Before matrix multiplication, the PTRE is used to reshape features. Thus, pixel-wise tokens are aggregated and converted into patch-wise tokens.

I. INTRODUCTION

Salient object detection (SOD) aims to identify the most significant objects or regions in images or videos from various visual scenes. It plays a fundamental and important role in many computer vision tasks, such as semantic segmentation [1], medical image segmentation [2], [3] video object segmentation [4]–[6], person re-identification [7], object tracking [8], [9] and recognition [10], image editing [11] and compression [12].

Although many purely CNN-based methods [13]–[17] achieve quite promising results on the RGB SOD task, they still struggle with challenges of complex or low-contrast scenes, and obscured or indistinguishable objects. To this end, some recent researches have attempted to introduce additional information, such as the depth signal, to make the model comfortable with complicated and diverse natural scenes. The depth map can explicitly provide complementary spatial structure information and the relative position relationship between objects, which helps to distinguish different objects and alleviate the above issues. Therefore, recent research is gradually shifting towards the integration of modality-specific and modality-complementary cues from RGB and depth images to excavate and capture objects of interest. At the same time, long-range context and contrast information play a key role in identifying and locating salient objects. However, the purely convolution-based architectures¹ possibly encounter the performance bottleneck, which is caused by the localized convolution operation and the fixedness of the learned

parameters. Hence, the introduction of a new architecture becomes more and more important.

The transformer [18] has superior performance against existing state-of-the-art CNNs in several computer vision tasks [19], [20], which can be attributed to its powerful ability of extracting feature and modeling long-range dependencies. In this paper, we introduce the transformer to design a simple yet effective RGB-D SOD model, TransCMD. A novel transformer-based top-down multi-level structure is engineered for the cross-modal fusion, which can be easily assembled to a CNN feature extractor, like VGG [21] and ResNet [22]. We leverage the self- and cross-attention to learn feature alignment where each element gathers information from other elements in the global sequence based on semantic similarity. This can naturally achieve the transformation and enhancement of intra-modal features and the matching and fusion of inter-modal features. However, a prominent problem of the transformer is the unbearable quadratic computational complexity caused by the attention operation based on all elements of the feature map. To cope with this, we introduce the patch embedding in the attention block. Instead of using patch-embedding to extract and compress image features in the input stage [19] or at each feature scale [20], we apply it to compute each matrix multiplication of self- and cross-attention with the pixel-wise tokens as the input. We call it “patch-wise token re-embedding” (PTRE) as shown in Fig. 1. When learning multi-scale and high-resolution features, such a design can reduce computation and memory costs by a factor of p^2 and p^4 (p is the side length of the patch), respectively. And, the proposed components together with the convolutional feed forward network can effectively

¹Manuscript version.

¹Their core components are the convolution, which are different from our transformer-based structure.

characterize global and local information.

Our contributions can be summarized as:

- We introduce the transformer to rethink the SOD modeling from a sequence-to-sequence perspective, which gains better interpretability.
- We construct a top-down transformer-based information propagation path (TIPP), which can align the CNN features of RGB and depth modalities and fully exploit the inter-modal complementary information.
- We boost the matrix operation in the attention by using the patch-wise token re-embedding (PTRE), which improves the efficiency of the transformer for multi-scale and high-resolution features. And aided by the convolutional feed forward network, the locality of features can be further enhanced, and key cues in both global and local contexts can be fully perceived and explored.
- Extensive experiments demonstrate that the proposed model outperforms sixteen purely CNN-based methods on seven RGB-D SOD datasets.

II. RELATED WORK

a) Visual Attention.: Humans can quickly capture significant objects or regions in a scene. The modeling and investigation of such an ability is a fundamental and critical problem in computer vision, i.e. visual attention mechanism. Researches in this area can be divided into two different directions: one is to explore where the observer is looking, i.e. eye fixation prediction (FP) [23], and the other is to locate and segment completely visually attractive regions, i.e. salient object detection (SOD) [24], [25]. In this paper, we focus on the latter. With the FCN-like [26] and UNet-like [27] architectures becoming the dominant paradigm for SOD, the proliferation of CNN-based methods has driven the rapid development of SOD in recent years [28], [29].

b) RGB-D Salient Object Detection.: RGB-D SOD introduces the depth map to supplement spatial information for RGB data, which can provide a more comprehensive understanding of the scene. Roughly speaking, the existing methods can be broadly classified into three categories depending on the cross-modal fusion strategy: early fusion, intermediate fusion, and late fusion. **Early fusion** methods directly combine the low-level information of two modalities, e.g., concatenating the inputs [30]–[32] or integrating their low-level features [33]. Although such a scheme may reduce the number of model parameters, it also leads to very difficultly control the interference of the noise within different modalities to the overall model. Unlike early fusion, **late fusion** methods generally adopt a dual-stream structure and focus more on the cross-modal fusion of high-level features [34]–[36] or final predictions [37]. Since the semantic information enriched by high-level features has a positive guide for good prediction results, late fusion methods are dominated. In fact, both low-level and high-level features have the same importance in the SOD task, and they complement each other. The low-level features can provide rich texture and structural scene perception, which is missing in the high-level features. Hence, an **intermediate fusion** strategy that utilizes both simultaneously is gradually

becoming the mainstream of RGB-D SOD methods [38]–[47]. Our proposed method can also be classified in this category. These algorithms construct various cross-modal interaction strategies based on the CNN structures, which typically draw on the plug-and-play modules or their variants to enhance and rectify the representation of features such as ASPP [48] or DenseASPP [49] ([31], [35], [42], [44]–[46], [50]), and ConvLSTM [51] ([42]). Unlike them, we introduce a global sequence perspective for feature enhancement and interaction. This can effectively fill the lack of contextual information caused by the local reception field of the convolution operation.

c) Attention-Based Model.: On the one hand, as mentioned earlier, the attention mechanism is closely related to the SOD task. Some methods [35], [42], [44], [50] apply channel and spatial attention [52], [53] and dynamic convolution [54]. Although these data-adaptive feature enhancement methods in spatial or channel form can improve the flexibility and expressiveness of the model, these convolution-based strategies do not model long-range dependencies well and still have a large room for improvement. Another related work [45] introduces the non-local block [55], but it is only used to enhance feature interaction in the topmost layer, and the model body is still limited by the CNN architecture. In contrast, our approach achieves further exploration by thoroughly building the multi-level cross-modal fusion scheme on a sequence-to-sequence [18] transformation perspective. On the other hand, the transformer [18] is built on the attention mechanism, which has shown powerful performance in natural language processing, is receiving more and more interest from researchers in computer vision. The recent remarkable performance of vision transformers [19], [20], [56] reflects that the transformer is a general and effective architecture to transform features. Most of them use the transformer to extract image features for the classification task. SETR [57] is a pioneering work of applying transformer to the segmentation field and it uses ViT [19] to extract features and builds a lightweight convolutional decoder to obtain predictions. Similar to it, in fact, the existing methods tend to explore the application of transformer in the encoder, and there is little work focusing on the decoder. In the segmentation task, the decoder plays an important role and both transformer-based encoder and decoder are worthy of being explored. So different from the existing methods which propose the transformer-based encoder, our work is more inclined to explore the design of the transformer-based decoder, especially for cross-modal tasks such as RGB-D SOD. We use it to decode the CNN features and build an encoder-decoder architecture for the RGB-D SOD task and this work and the existing methods can complement each other. In addition, we apply the transformer to multi-scale high-resolution features, which faces the computational pressure of higher resolution features. Also, since RGB-D SOD requires considering two modalities, their integration is one of the key points of our model design.

III. OUR METHOD: TRANSCMD

In this paper, we propose a simple yet effective cross-modal feature integration network based on the transformer. In the

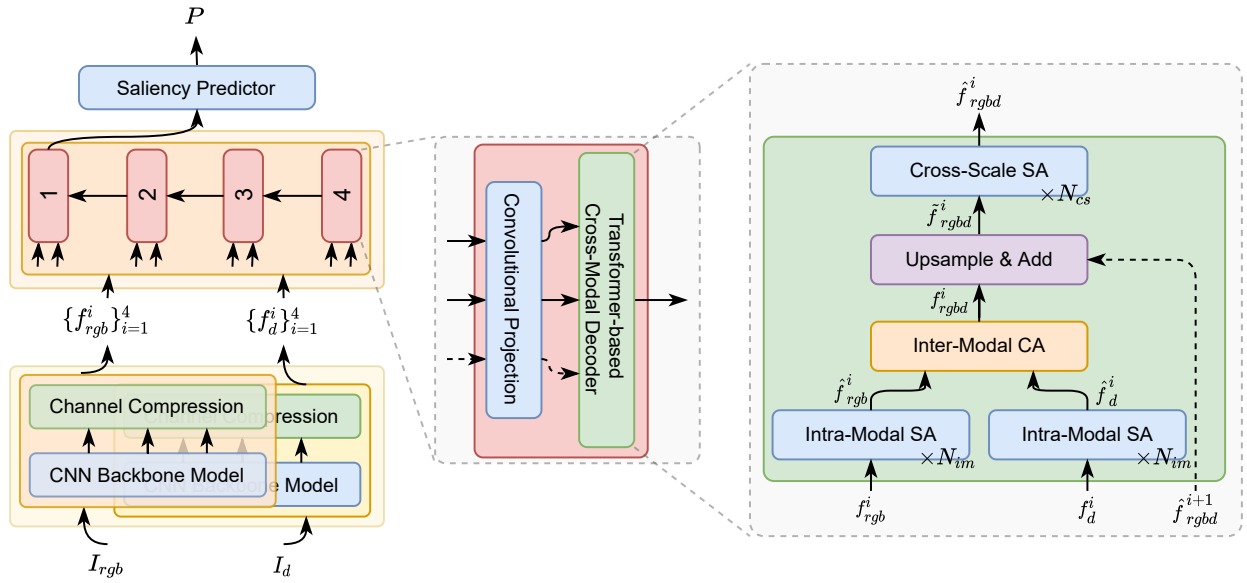


Fig. 2. The overview of the proposed model. “ N_{im} ” and “ N_{cs} ” represent the number of the stacked intra-modal and cross-scale SA blocks in the TIPP and default values are 2 and 1, respectively. Note that the dashed arrow denotes an optional input for the decoder, and in our model, the 4th decoder block contains only two inputs, i.e. f_{rgb}^4 and f_d^4 . The feature \hat{f}_{rgb}^{i+1} is upsampled using bilinear interpolation in the 2D form.

following, we first show the overview of the model, and then describe the details of each component.

A. Network Overview

In our approach, widely used CNNs, i.e. VGG [21] or ResNet [22], act as the feature encoder network for two modalities: RGB and depth. As shown in Fig. 2, the features with different scales from each intermediate layer of the backbone are independently passed through a simple lateral connection structure to compress the channels, which aims to obtain more compact features $\{f_{rgb}^i\}_{i=1}^4$ from the RGB image I_{rgb} and $\{f_d^i\}_{i=1}^4$ from the depth image I_d , and reduce the memory cost. These multi-scale features abound with the cues about appearances, boundaries, textures, and more complex semantic concepts from the RGB modality, and relative spatial location relationships between objects from the depth modality. They are fed into the proposed transformer-based information propagation path (TIPP). By absorbing shallow features from top to down, this serialized cross-modal information aggregation process gradually recovers the high-resolution representation. And the salient object regions are enriched and shaped. Eventually, the refined features are mapped as the final single-channel saliency map \mathcal{P} , through the bilinear interpolation and a simple convolution layer with a sigmoid activation. It is supervised by the binary ground truth \mathcal{G} .

B. TIPP: Transformer-based Information Propagation Path

The TIPP is proposed mainly to process and integrate top-down features from both RGB and depth modalities with different scales, which consists of four cascaded cross-modal integration units (CMIUs), as shown in Fig. 2. Among them, the 4th CMIU is only responsible for the integration of cross-modal information. It takes feature maps f_{rgb}^4 and f_d^4 with

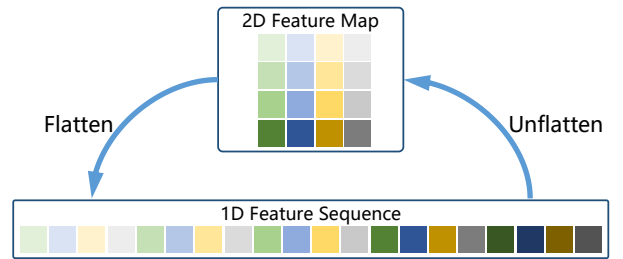


Fig. 3. Conversion between the 2D feature map and the 1D feature sequence.

the same scale as input. While each of the remaining CMIUs needs to additionally integrate the output feature map from the adjacent higher level. In addition, each input map of the CMIU needs to be converted into a D -dimensional pixel-wise embedding map in a separate embedding layer. Before the integration of modalities through the inter-modal cross attention block, f_{rgb} and f_d are first reconstructed and self-reinforced by N_{im} stacked intra-modal self-attention blocks, respectively. For the following N_{cs} cross-scale self-attention blocks, if there exists the feature \hat{f}_{rgb}^{i+1} from the previous CMIU, the input is the sum of the upsampled \hat{f}_{rgb}^{i+1} and the output f_{rgb}^i of the cross-attention block, otherwise, the input is only f_{rgb}^i . The resolution of \hat{f}_{rgb}^1 is half of that of the input I_{rgb} and I_d .

C. Intra-Modal / Cross-Scale Self-Attention

The intra-modal and cross-scale self-attention blocks play different roles, but their structures are the same. The specific details of the self-attention block can be found in Fig. 4a, which is characterized by a patch-wise multi-head self-attention (PMHSA), a convolutional feed forward network (CFFN), normalization layers, dropout layers and residual connectors. The PMHSA follows a pre-normalization [58], [59] layer and

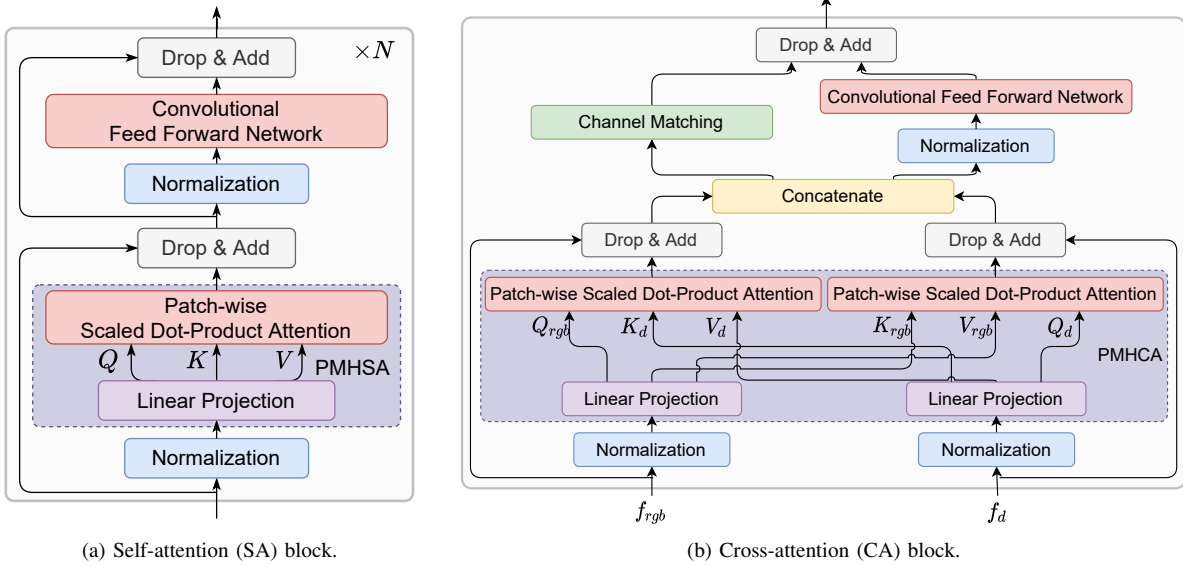


Fig. 4. Attention blocks of the proposed network.

they are wrapped by a residual connector. The output is then passed to a pre-normalized CFFN whose input and output are similarly connected in a residual way. Moreover, a dropout operation is also applied to the output of the PMHSA or the CFFN. The overall process can be expressed as:

$$\begin{aligned} X &= \text{Dropout}(\text{PMHSA}(\text{Norm}(X))) + X, \\ X &= \text{Dropout}(\text{CFFN}(\text{Norm}(X))) + X, \end{aligned} \quad (1)$$

where $X \in \mathbb{R}^{N \times D}$ refers to the flattened image features. $N = H \times W$ and D denote the number of tokens (or pixels) and the embedding dimension.

a) Multi-Head Self-Attention (MHSA).: At first, we introduce its original form of in the transformer [18]. This operation is actually a feature alignment process, which computes the feature correlation to reconstruct the query itself. And a single head of it can be defined as:

$$\begin{aligned} Y_h &= \text{Softmax}\left(\frac{Q_h K_h^\top}{\alpha}\right) V_h, \\ [Q_h, K_h, V_h] &= X[\mathbf{W}_q, \mathbf{W}_k, \mathbf{W}_v], \end{aligned} \quad (2)$$

where Q_h, K_h, V_h are a single head of query, key and value, respectively. $\mathbf{W}_q, \mathbf{W}_k, \mathbf{W}_v \in \mathbb{R}^{D \times D/N_h}$ are the corresponding projection matrices. N_h is the number of heads and $\alpha = \sqrt{D/N_h}$ is a scaling factor. The outputs from different heads are concatenated together and fused by a dense layer. The final output $Z \in \mathbb{R}^{N \times D}$ can be expressed as $Z = \text{Dropout}([Y_1, \dots, Y_{N_h}] \mathbf{W}_o)$ and $\mathbf{W}_o \in \mathbb{R}^{D \times D}$ is an output projection layer. It is noted that the dot product operation in the attention matrix $Q_h K_h^\top$ has a quadratic complexity w.r.t. the input sequence length, i.e. N^2 , which limits it to handling multi-scale high-resolution features. We introduce the patch-wise re-embedding to alleviate the issue and propose the patch-wise multi-head self-attention.

b) Patch-wise Multi-Head Self-Attention (PMHSA).: The PMHSA improves the matrix operation from the pixel-wise form to the patch-wise form compared with the MHSA, which

reduces the complexity by a factor of p^2 . Here, p^2 is the number of elements in a patch. Specifically, Q_h, K_h and V_h in Equ. 2 are unflattened to the 2D form (Fig. 3) and performed the patch-wise token re-embedding (PTRE) operation. In the PTRE, the map with D/N_h -dimensional embedding is unfolded to $N/p^2 \times Dp^2/N_h$ (Fig. 1). After the operation in Equ. 2, the patch-wise result is reshaped back to $N \times D/N_h$ and subsequent operations are consistent with those of the MHSA.

c) Convolutional Feed Forward Network (CFFN).:

Although the transformer can better model the long-range interaction, the local correlation still has a strong practical value as a kind of inductive bias for image data in the vision task. The original position-wise feed forward network (FFN) in the transformer only performs separate channel transformations for each element of the sequence, which lacks attention to the local context. Hence, we adapt the FFN by using the convolution operation. The original two fully-connected layers are replaced with the common combination of “ 3×3 convolution \rightarrow batch normalization \rightarrow activation” and finally a 1×1 convolution layer is utilized to obtain the feature with the same dimension as the output of the original FFN.

D. Inter-Modal Cross-Attention

The inter-modal cross-attention block (Fig. 4b) is used to associate and interact information between modalities. Its input is from the outputs of two separated intra-modal self-attention blocks. Similar to the self-attention block, the input features are also normalized. Then, they are passed into the patch-wise multi-head cross-attention (PMHCA) for cross-modal alignment and enhancement, and are regularized by the dropout layer. Next, the features from two modality streams are concatenated and then locally enhanced by the CFFN followed by a dropout. In the skip connection, a simple linear layer is applied to match the channel dimension. Finally, the output is the sum of the two results.

TABLE I

COMPARISON WITH EXISTING STATE-OF-THE-ART RGB-D SOD METHODS. †: VGG-16 [21] AS THE BACKBONE; ‡: VGG-19 [21] AS THE BACKBONE; †: RESNET-50 [22] AS THE BACKBONE; ‡: RESNET-101 [22] AS THE BACKBONE; —: UNAVAILABLE RESULTS. THE BEST THREE RESULTS ARE HIGHLIGHTED USING RED, GREEN AND BLUE IN THAT ORDER. PLEASE ZOOM IN FOR A CLEARER VIEW.

METHODS	CTMF† [34] 2018	PCANet† [38] 2018	CPFP† [41] 2019	MMCI† [40] 2019	TANet† [39] 2019	DMRA† [42] 2019	DisenFuse† [36] 2020	CMWNet† [43] 2020	S2MA† [45] 2020	D3Net† [32] 2020	ICNet† [60] 2020	UCNet† [50] 2020	DANet† [31] 2020	HDFNet‡ [35] 2020	JLDCF‡ [46] 2020	CoNet‡ [44] 2020	Ours† 2021	Ours‡ 2021	
DUTRGBD [42]	S_m	0.831	0.801	0.749	0.791	0.808	0.888	0.798	0.887	0.903	0.775	0.852	0.864	0.899	0.907	0.905	0.919	0.923	0.932
	F_{β}	0.681	0.687	0.637	0.627	0.704	0.851	0.690	0.831	0.862	0.668	0.784	0.820	0.860	0.864	0.863	0.890	0.891	0.906
	MAE	0.097	0.100	0.100	0.112	0.093	0.048	0.104	0.056	0.044	0.097	0.072	0.057	0.043	0.041	0.043	0.034	0.034	0.030
	F_{β}^{adv}	0.792	0.760	0.735	0.753	0.779	0.882	0.750	0.866	0.885	0.756	0.830	0.855	0.888	0.885	0.883	0.908	0.908	0.920
	F_{β}^{max}	0.823	0.771	0.718	0.767	0.790	0.897	0.774	0.888	0.900	0.742	0.850	0.857	0.906	0.918	0.911	0.927	0.926	0.938
	E_m^{adv}	0.882	0.863	0.815	0.856	0.871	0.930	0.854	0.922	0.935	0.849	0.901	0.906	0.937	0.938	0.938	0.952	0.949	0.957
	E_m^{max}	0.899	0.856	0.810	0.859	0.861	0.933	0.855	0.926	0.937	0.833	0.899	0.904	0.940	0.947	0.943	0.956	0.955	0.962
	E_m^{max}	0.849	0.877	0.878	0.859	0.878	0.886	0.889	0.903	0.894	0.900	0.894	0.897	0.899	0.908	0.902	0.896	0.918	0.925
NIUD [61]	S_m	0.849	0.801	0.749	0.791	0.808	0.888	0.798	0.887	0.903	0.775	0.852	0.864	0.899	0.907	0.905	0.919	0.923	0.932
	F_{β}	0.720	0.803	0.828	0.739	0.803	0.846	0.831	0.857	0.842	0.854	0.843	0.868	0.857	0.877	0.869	0.848	0.874	0.883
	MAE	0.085	0.059	0.053	0.079	0.061	0.051	0.052	0.046	0.053	0.046	0.052	0.043	0.045	0.038	0.041	0.046	0.039	0.034
	F_{β}^{adv}	0.788	0.844	0.837	0.813	0.844	0.871	0.859	0.880	0.865	0.865	0.868	0.889	0.871	0.889	0.885	0.872	0.892	0.898
	F_{β}^{max}	0.845	0.872	0.877	0.853	0.874	0.886	0.886	0.902	0.889	0.900	0.891	0.895	0.898	0.911	0.904	0.893	0.919	0.929
	E_m^{adv}	0.866	0.909	0.900	0.882	0.909	0.920	0.900	0.923	0.916	0.916	0.913	0.934	0.922	0.932	0.935	0.924	0.932	0.941
	E_m^{max}	0.913	0.924	0.923	0.915	0.925	0.927	0.928	0.936	0.930	0.939	0.926	0.936	0.935	0.944	0.944	0.937	0.951	0.958
	E_m^{max}	0.860	0.874	0.884	0.856	0.886	0.899	0.900	0.917	0.915	0.912	0.923	0.920	0.915	0.923	0.925	0.908	0.927	0.924
NLPR [30]	S_m	0.679	0.762	0.807	0.676	0.779	0.838	0.828	0.856	0.852	0.849	0.864	0.878	0.862	0.882	0.882	0.841	0.867	0.867
	F_{β}	0.056	0.044	0.038	0.059	0.041	0.031	0.035	0.029	0.030	0.030	0.028	0.025	0.028	0.023	0.022	0.031	0.026	0.030
	MAE	0.724	0.795	0.818	0.730	0.795	0.853	0.839	0.859	0.853	0.861	0.870	0.890	0.870	0.889	0.878	0.845	0.869	0.869
	F_{β}^{adv}	0.825	0.841	0.862	0.815	0.863	0.879	0.881	0.903	0.902	0.897	0.908	0.903	0.903	0.917	0.918	0.887	0.916	0.913
	F_{β}^{max}	0.869	0.916	0.920	0.872	0.916	0.941	0.933	0.940	0.942	0.945	0.945	0.955	0.949	0.957	0.955	0.933	0.949	0.947
	E_m^{adv}	0.929	0.925	0.929	0.913	0.941	0.947	0.944	0.951	0.953	0.953	0.952	0.956	0.953	0.963	0.963	0.945	0.963	0.958
	E_m^{max}	0.863	0.843	0.872	0.848	0.858	0.900	0.877	0.934	0.941	0.898	0.920	0.933	0.924	0.926	0.931	0.910	0.937	0.938
	E_m^{max}	0.686	0.710	0.787	0.650	0.738	0.842	0.779	0.888	0.892	0.829	0.867	0.908	0.877	0.895	0.894	0.848	0.892	0.891
RGBD135 [62]	S_m	0.055	0.050	0.038	0.065	0.046	0.030	0.040	0.022	0.021	0.031	0.027	0.018	0.023	0.021	0.020	0.028	0.021	0.021
	F_{β}	0.778	0.774	0.829	0.762	0.795	0.865	0.820	0.900	0.906	0.870	0.889	0.917	0.899	0.912	0.900	0.870	0.911	0.909
	MAE	0.844	0.802	0.846	0.822	0.828	0.888	0.845	0.930	0.935	0.885	0.913	0.930	0.914	0.921	0.923	0.896	0.932	0.934
	F_{β}^{adv}	0.911	0.911	0.927	0.904	0.919	0.944	0.923	0.967	0.974	0.951	0.959	0.974	0.968	0.971	0.969	0.945	0.976	0.974
	F_{β}^{max}	0.932	0.891	0.923	0.928	0.910	0.942	0.921	0.969	0.973	0.945	0.960	0.976	0.966	0.970	0.968	0.945	0.975	0.976
	E_m^{adv}	0.716	0.842	0.850	0.833	0.835	0.806	0.859	0.867	0.872	0.860	0.854	0.875	0.875	0.886	0.880	0.858	0.891	0.901
	F_{β}	0.535	0.768	0.788	0.712	0.748	0.739	0.780	0.811	0.819	0.799	0.791	0.836	0.822	0.848	0.844	0.802	0.837	0.858
	MAE	0.139	0.071	0.064	0.086	0.075	0.086	0.068	0.062	0.057	0.063	0.069	0.051	0.054	0.047	0.049	0.063	0.050	0.043
SIP [32]	S_m	0.684	0.825	0.819	0.795	0.809	0.818	0.819	0.851	0.854	0.835	0.836	0.868	0.855	0.875	0.873	0.841	0.866	0.885
	F_{β}	0.694	0.838	0.851	0.818	0.830	0.821	0.852	0.874	0.877	0.861	0.857	0.879	0.876	0.894	0.889	0.867	0.899	0.914
	MAE	0.824	0.900	0.899	0.886	0.894	0.863	0.899	0.909	0.913	0.902	0.900	0.918	0.915	0.924	0.923	0.909	0.923	0.935
	F_{β}^{adv}	0.829	0.901	0.903	0.897	0.895	0.874	0.911	0.913	0.919	0.909	0.903	0.919	0.918	0.930	0.925	0.913	0.933	0.943
	F_{β}^{max}	0.776	0.843	0.807	0.814	0.839	0.857	—	0.875	0.868	0.857	0.848	—	0.864	0.879	—	0.853	0.880	0.894
	E_m^{adv}	0.621	0.731	0.708	0.661	0.726	0.784	—	0.795	0.787	0.777	0.772	—	0.795	0.821	—	0.779	0.802	0.822
	E_m^{max}	0.100	0.063	0.082	0.082	0.063	0.059	—	0.051	0.052	0.058	0.064	—	0.050	0.045	—	0.060	0.050	0.040
	E_m^{max}	0.709	0.785	0.726	0.748	0.766	0.820	—	0.820	0.818	0.814	0.799	—	0.827	0.842	—	0.805	0.826	0.841
SSD [63]	S_m	0.729	0.811	0.766	0.782	0.810	0.844	—	0.871	0.848	0.834	0.841	—	0.843	0.870	—	0.840	0.865	0.879
	F_{β}	0.838	0.889	0.832	0.860	0.886	0.898	—	0.902	0.898	0.904	0.879	—	0.911	0.911	—	0.898	0.901	0.913
	MAE	0.864	0.899	0.852	0.883	0.897	0.906	—	0.930	0.909	0.910	0.902	—	0.914	0.925	—	0.915	0.920	0.929
	F_{β}^{adv}	0.776	0.843	0.807	0.814	0.839	0.857	—	0.875	0.868	0.857	0.848	—	0.864	0.879	—	0.853	0.880	0.894
	F_{β}^{max}	0.621	0.731	0.708	0.661	0.726	0.784	—	0.795	0.787	0.777	0.772	—	0.795	0.821	—	0.779	0.802	0.822
	E_m^{adv}	0.100	0.063	0.082	0.082	0.063	0.059	—	0.051	0.052	0.058	0.064	—	0.050	0.045	—	0.060	0.050	0.040
	E_m^{max}	0.709	0.785	0.726	0.748	0.766	0.820	—	0.820	0.818	0.814	0.799	—	0.827	0.842	—	0.805	0.826	0.841
	E_m^{max}	0.838	0.889	0.832	0.860	0.886	0.898	—	0.902	0.898	0.904	0.879	—	0.911	0.911	—	0.898	0.901	0.913
STERE [64]	S_m	0.848	0.875	0.879	0.873	0.871	0.752	0.883	0.905	0.890	0.899	0.903	0.903	0.901	0.900	0.903	0.905	0.908	0.912
	F_{β}	0.698	0.778	0.817	0.760	0.787	0.647	0.811	0.847	0.825	0.838	0.844	0.867	0.846	0.853	0.857	0.865	0.847	0.854
	MAE	0.086	0.064	0.051	0.068	0.060	0.087	0.054	0.043	0.051	0.046	0.045	0.039	0.043	0				

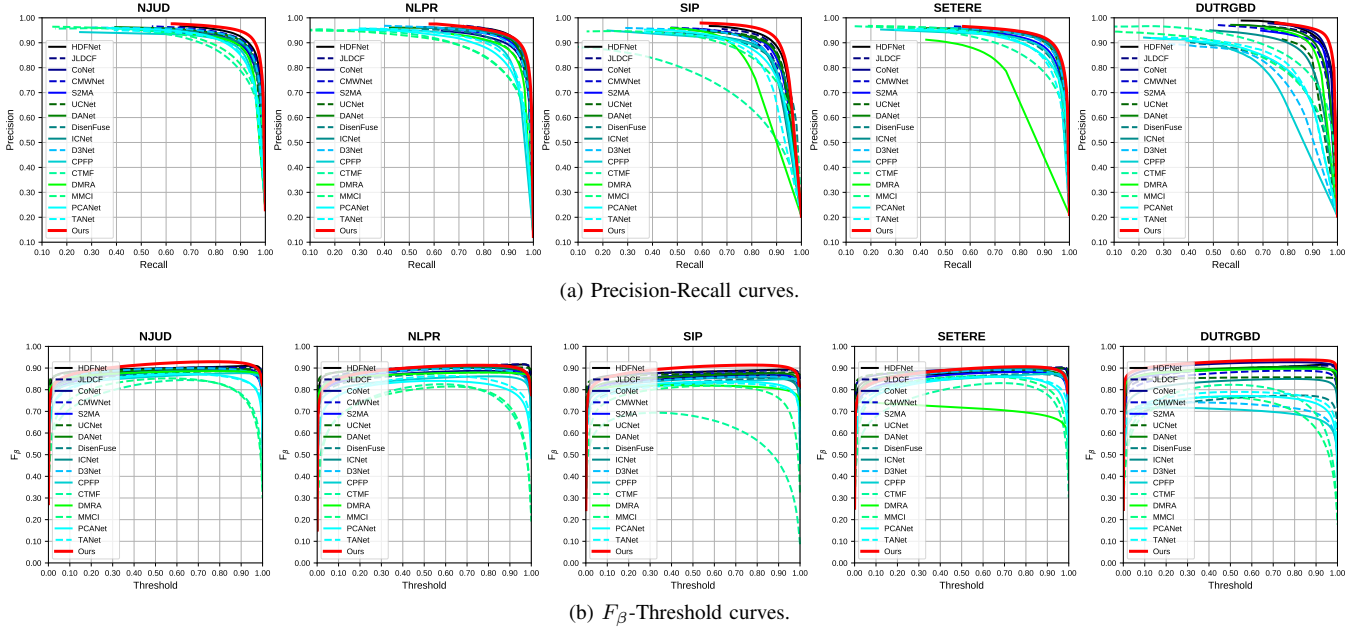


Fig. 5. PR and F_β curves of the proposed model and 16 state-of-the-art algorithms over five RGB-D SOD datasets.

NLPR and 1485 images from NJUD as the training set, and the remaining data of these datasets except DUTRGBD as the testing set. For DUTRGBD, the proposed model is trained on 800 images and tested on the remaining 400 images.

B. Evaluation Metrics.

To fully demonstrate the performance differences of different methods, we introduced 9 metrics to quantitatively evaluate the models. Specifically, **S-measure** [65] (S_m) focuses on region-aware and object-aware structural similarities between the saliency map and the ground truth. **MAE** [66], (MAE) indicates the average absolute pixel error. **F-measure** [67] (F_β) is a region-based similarity metric and based on precision and recall. **E-measure** [68] (E_m) is characterized as both image-level statistics and local pixel matching. F_β and E_m rely on specific thresholds to binarize prediction maps and the adaptive version F_β^{adp} and E_m^{adp} can be obtained when twice the average of the saliency probability map is used as the threshold. If F_β and E_m are calculated using a series of binary maps corresponding to thresholds varying from 0 to 255, we can plot their curves w.r.t. the threshold. The maximums of the F_β curve and the E_m curve are F_β^{max} and E_m^{max} , respectively. And the series of paired precision and recall values used to calculate F_β can form **PR curve**. **Weighted F-measure** [69] (F_β^ω) improves the metric F_β by using a weighted precision for measuring exactness and a weighted recall for measuring completeness.

C. Implementation Detail

As shown in Fig. 2, we stack N_{im} intra-modal self-attention blocks and N_{cs} cross-scale self-attention blocks in the CMIU. The ablation analysis of N_{im} and N_{cs} can be found in ablation studies. If not specified, N_{im} and N_{cs} are set to 2 and 1 by default.

The backbone network is initialized by the weight of VGG-16 [21] or ResNet-101 [22] pre-trained on ImageNet, and the remaining structures are initialized randomly using the default method of the PyTorch toolbox. All our models are trained for 22K steps with a batch size of 4 using a momentum SGD optimizer with a momentum of 0.9 and a weight decay of 0.0005 on an NVIDIA GTX 2080Ti GPU. The learning rate is initialized as 0.005 and scheduled by the ‘‘poly’’ strategy with a factor of 0.9. And the dropout regularization technology with the probability of 0.1 is applied for all attention blocks to avoid over-fitting. The single-channel depth input is repeated three times along the channel dimension to facilitate the use of pre-trained parameters, and RGB and depth images are resized to 256×256 . All RGB-D image pairs are augmented by random horizontal flipping and random rotating, and random color jittering and normalization are only used for RGB images. In the testing stage, the normalized RGB and repeated depth images are resized to 256×256 and the final prediction is resized back to the original size for evaluation. For all experiments, the model is supervised by the binary cross entropy loss. And we also supplement the results of the model based on the hybrid loss [13], [50] in ablation studies.

D. Comparison

To demonstrate the effectiveness of our method, we compare it with the recent 16 state-of-the-art RGB-D SOD methods, including CoNet [44], JLDCF [46], HDFNet [35], DANet [31], UCNet [50], ICNet [60], D3Net [32], S2MA [45], CMWNet [43], DisenFuse [36], DMRA [42], TANet [39], MMCI [40], CFPF [41], PCANet [38] and CTMF [34]. They are all based on deep learning and CNN architecture. All data used in experiments are from the resources released by the authors.

a) *Quantitative Comparison.*: In Tab. I, the detailed results from all competitors on seven datasets and nine metrics

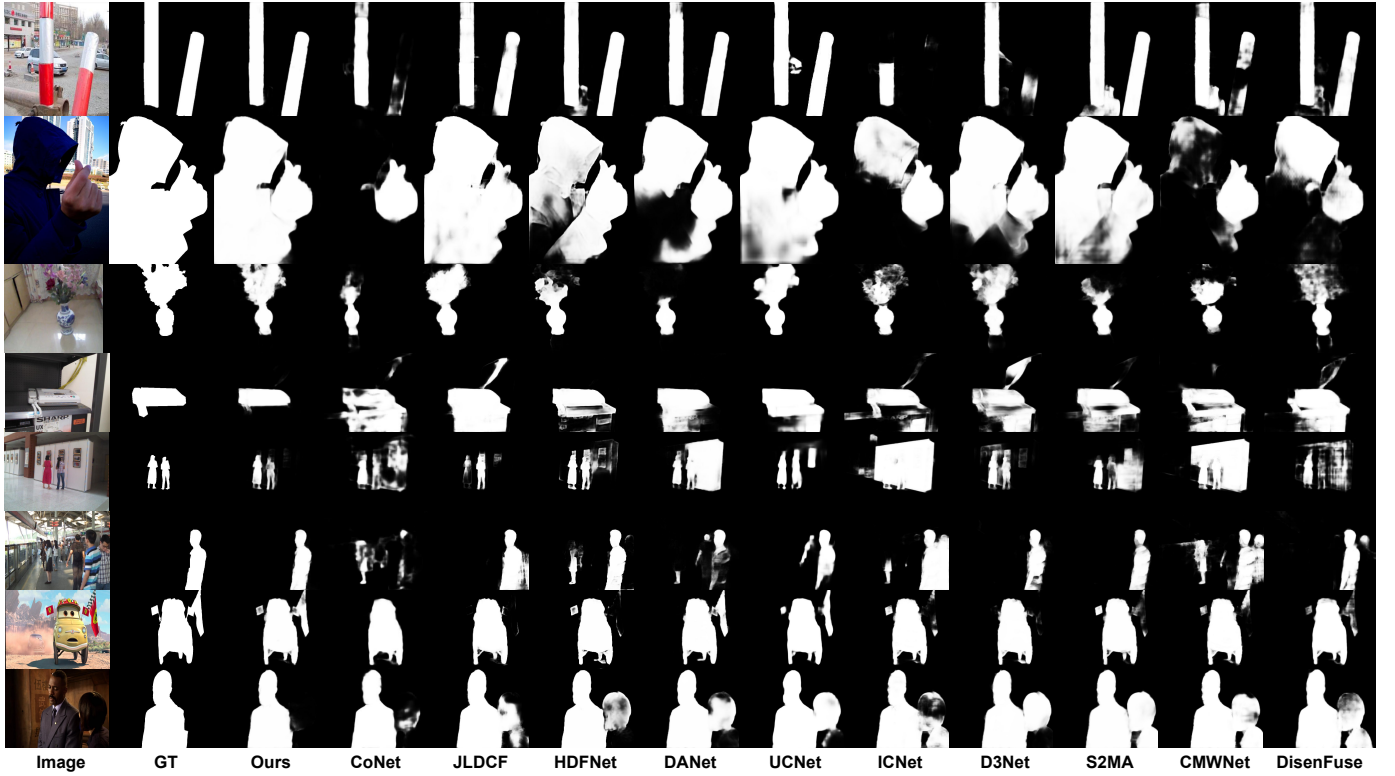


Fig. 6. Qualitative comparison of our model with ten recent state-of-the-art models.

TABLE II

ABLATION ANALYSIS OF THE DIFFERENT COMPONENTS. HERE, THE ‘‘PVT-STYLE PATCH-WISE EMBEDDING’’ REFERS TO THE PATCH EMBEDDING IS APPLIED TO THE INPUT OF DIFFERENT CMIUS.

No.	Proj.	FFN	Pos.	NJUD					NLPR					SIP					STERE				
				S_m	F_{β}^{ω}	MAE	F_{β}^{adp}	E_m^{adp}	S_m	F_{β}^{ω}	MAE	F_{β}^{adp}	E_m^{adp}	S_m	F_{β}^{ω}	MAE	F_{β}^{adp}	E_m^{adp}	S_m	F_{β}^{ω}	MAE	F_{β}^{adp}	E_m^{adp}
1	\times	\times	\times	0.901	0.847	0.046	0.872	0.920	0.915	0.847	0.031	0.854	0.940	0.866	0.801	0.062	0.847	0.905	0.882	0.815	0.052	0.859	0.920
with PVT-style patch-wise embedding																							
2.1	Lin.	Lin.	\checkmark	0.900	0.842	0.049	0.866	0.917	0.913	0.839	0.032	0.843	0.937	0.871	0.802	0.060	0.843	0.910	0.889	0.818	0.052	0.852	0.921
2.2	Lin.	Lin.	\times	0.906	0.852	0.045	0.876	0.922	0.913	0.840	0.032	0.846	0.937	0.873	0.802	0.059	0.842	0.910	0.890	0.819	0.051	0.852	0.920
with PETR																							
3.1	Lin.	Lin.	\checkmark	0.912	0.863	0.042	0.885	0.929	0.919	0.852	0.032	0.855	0.941	0.888	0.829	0.052	0.863	0.919	0.901	0.838	0.046	0.868	0.929
3.2	Lin.	Lin.	\times	0.918	0.874	0.039	0.892	0.932	0.921	0.859	0.028	0.860	0.943	0.883	0.827	0.053	0.862	0.917	0.907	0.848	0.043	0.872	0.931
3.3	Lin.	Conv.	\checkmark	0.917	0.871	0.041	0.889	0.929	0.921	0.863	0.028	0.867	0.945	0.884	0.830	0.052	0.864	0.917	0.904	0.841	0.045	0.869	0.930
3.4	Lin.	Conv.	\times	0.918	0.874	0.039	0.892	0.932	0.927	0.867	0.026	0.869	0.949	0.891	0.837	0.050	0.866	0.923	0.908	0.847	0.044	0.872	0.932
3.5	Conv.	Lin.	\times	0.911	0.862	0.042	0.880	0.924	0.921	0.857	0.029	0.860	0.944	0.880	0.819	0.054	0.853	0.917	0.900	0.835	0.047	0.864	0.928
3.6	Conv.	Conv.	\times	0.916	0.867	0.042	0.880	0.924	0.922	0.859	0.030	0.860	0.941	0.882	0.819	0.055	0.853	0.914	0.904	0.836	0.047	0.859	0.924

TABLE III

COMPARISON USING DIFFERENT NORMALIZATION LAYERS ON FOUR DATASETS.

MODELS	NJUD					NLPR					SIP					STERE				
	S_m	F_{β}^{ω}	MAE	F_{β}^{adp}	E_m^{adp}	S_m	F_{β}^{ω}	MAE	F_{β}^{adp}	E_m^{adp}	S_m	F_{β}^{ω}	MAE	F_{β}^{adp}	E_m^{adp}	S_m	F_{β}^{ω}	MAE	F_{β}^{adp}	E_m^{adp}
BatchNorm	0.918	0.874	0.039	0.892	0.932	0.927	0.867	0.026	0.869	0.949	0.891	0.837	0.050	0.866	0.923	0.908	0.847	0.044	0.872	0.932
LayerNorm	0.919	0.875	0.039	0.887	0.930	0.926	0.868	0.027	0.873	0.952	0.884	0.830	0.053	0.865	0.918	0.907	0.848	0.043	0.874	0.935

TABLE IV

ABLATION ANALYSIS OF THE SIZE OF THE PATCH RE-EMBEDDING IN THE PTRE.

SIZE	NJUD					NLPR					SIP					STERE				
	S_m	F_{β}^{ω}	MAE	F_{β}^{adp}	E_m^{adp}	S_m	F_{β}^{ω}	MAE	F_{β}^{adp}	E_m^{adp}	S_m	F_{β}^{ω}	MAE	F_{β}^{adp}	E_m^{adp}	S_m	F_{β}^{ω}	MAE	F_{β}^{adp}	E_m^{adp}
4 × 4	0.918	0.874	0.039	0.892	0.932	0.927	0.867	0.026	0.869	0.949	0.891	0.837	0.050	0.866	0.923	0.908	0.847	0.044	0.872	0.932
8 × 8	0.919	0.878	0.038	0.896	0.935	0.928	0.869	0.027	0.872	0.949	0.892	0.840	0.049	0.871	0.923	0.906	0.845	0.044	0.868	0.928
16 × 16	0.917	0.873	0.039	0.892	0.933	0.925	0.866	0.027	0.864	0.947	0.889	0.834	0.051	0.864	0.921	0.903	0.843	0.045	0.868	0.928

are listed and our method performs best on most datasets. In particular, our ResNet-based method achieves the best performance on DUTRGBD, NJUD, SIP, and SSD. Specifically, the average performance gain of our method on three datasets,

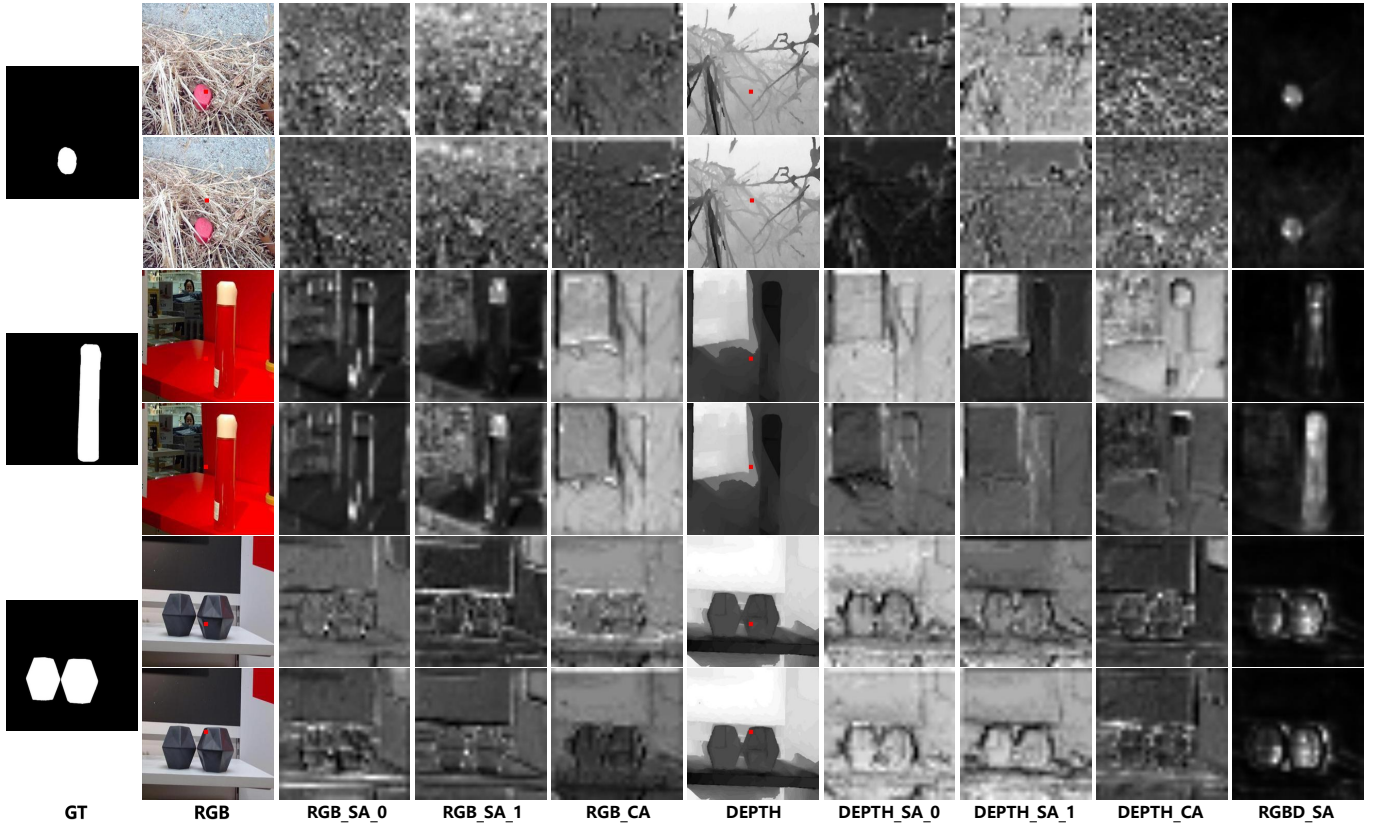


Fig. 7. Visualization of the attention maps from different attention operations in the 1st CMU. “*_SA_*i*” denotes the attention map from the *i*th SA block corresponding to the * modality. “*_CA” and “RGBD_SA” are from the specific stream in the CA block and the cross-scale SA block, respectively. Also, normalization and upsampling based on the bilinear interpolation are applied to show them more clearly. We choose the red square in the RGB and depth images to mark the positions in the query corresponding to the attention map and visually compare the attention maps of two different positions in the same image.

DUTRGBD, NJUD, and SIP, is significant, especially on the metric MAE , which is over 15% relative to the second-best method, HDFNet [35], and nearly 20% relative to the third-best method, JLDCE [46]. And it is also significantly competitive on other datasets. It is worth emphasizing that this work focuses on exploring and designing a new architecture suitable for RGB-D SOD. Therefore, the whole network is very simple and is not equipped with some other modules to further improve performance, such as ASPP, DenseASPP, and channel and spatial attention. When an additional loss that has been used in the works [13], [50] is introduced, the proposed model can yield more impressive performance, which is shown in Sec. IV-E0g. To compare the overall performance of different methods, we also show PR curves and F_β curves in Tab. 5. It can be seen that our method corresponds to a curve positioned more upward, which indicates that the proposed model performs better.

b) Qualitative Comparison.: Some visual comparisons of different models are listed in Fig. 6, which covers ten methods published in 2020. As we can see that these samples have various types of scenes and objects, including the multiple large or small objects (Row 1st and 5th), the large and out-of-bounds object in the high-contrast scene (Row 2nd), the medium-sized objects with unclear and complex boundaries (Row 3rd) or strong background interference (Row 4th, 6th and 8th) and the objects with large internal variability (Row

1st, 2nd and 7th). The results fully demonstrate the robustness of the proposed algorithm against different data, which can be attributed to the powerful information modeling capability of the attention mechanism.

E. Ablation Analysis

In order to evaluate the effectiveness of the proposed components and investigate their importance and contributions, we construct the ablation study on the NJUD, NLPR, SIP, and STERE datasets. At first, we build a CNN-based FPN-like two-stream model as the baseline network in which the features of the same resolution from both modalities are added directly. From the results in Tab. II we can see that it is a sufficiently strong baseline model, which also makes the gains from our approach more convincing. Besides, a linear version equipped with the proposed TIPP is constructed, which uses linear projection layers and FFNs. We also attach some other ablation analysis about the visualization of attention maps, the hybrid loss [13], [50], the comparison between LN [70] and BN [71], the setting of N_{im} and N_{cs} and some typical failure cases.

a) Positional Embedding (PE).: When the CNN is taken as the encoder, the zero padding operation means that the position information is already implicitly encoded in features [72], which makes the explicit PE unnecessary. In Tab. II,

TABLE V
ABLATION ANALYSIS ON THE NUMBER OF CMIU INTEGRATED INTO THE DECODER FROM SHALLOW TO DEEP.

Number	NJUD					NLPR					SIP					STERE				
	S_m	F_β^ω	MAE	F_β^{adp}	E_m^{adp}	S_m	F_β^ω	MAE	F_β^{adp}	E_m^{adp}	S_m	F_β^ω	MAE	F_β^{adp}	E_m^{adp}	S_m	F_β^ω	MAE	F_β^{adp}	E_m^{adp}
4	0.918	0.874	0.039	0.932	0.892	0.927	0.867	0.026	0.949	0.869	0.891	0.837	0.050	0.923	0.866	0.908	0.847	0.044	0.932	0.872
3	0.913	0.869	0.040	0.931	0.887	0.923	0.864	0.029	0.949	0.870	0.883	0.829	0.053	0.917	0.860	0.905	0.845	0.044	0.930	0.870
2	0.913	0.867	0.041	0.929	0.885	0.923	0.863	0.028	0.945	0.862	0.886	0.827	0.051	0.919	0.855	0.903	0.845	0.044	0.930	0.868
1	0.909	0.861	0.043	0.926	0.882	0.921	0.856	0.030	0.944	0.858	0.882	0.823	0.053	0.918	0.855	0.900	0.837	0.046	0.929	0.864
0	0.901	0.847	0.046	0.920	0.872	0.915	0.847	0.031	0.940	0.854	0.866	0.801	0.062	0.905	0.847	0.882	0.815	0.052	0.920	0.859

TABLE VI
ABLATION ANALYSIS OF THE NUMBER OF INTRA-MODAL AND CROSS-SCALE SELF-ATTENTION BLOCKS.

N_{im}	N_{cs}	NJUD					NLPR					SIP					STERE				
		S_m	F_β^ω	MAE	F_β^{adp}	E_m^{adp}	S_m	F_β^ω	MAE	F_β^{adp}	E_m^{adp}	S_m	F_β^ω	MAE	F_β^{adp}	E_m^{adp}	S_m	F_β^ω	MAE	F_β^{adp}	E_m^{adp}
0	1	0.916	0.872	0.040	0.891	0.932	0.929	0.874	0.026	0.871	0.949	0.881	0.825	0.056	0.860	0.913	0.908	0.848	0.043	0.872	0.932
1	0	0.914	0.869	0.040	0.880	0.928	0.920	0.859	0.030	0.864	0.946	0.881	0.824	0.052	0.853	0.918	0.902	0.843	0.044	0.866	0.931
1	1	0.917	0.873	0.040	0.889	0.928	0.922	0.861	0.029	0.865	0.945	0.886	0.831	0.052	0.865	0.917	0.907	0.849	0.044	0.874	0.932
1	2	0.916	0.872	0.040	0.890	0.931	0.920	0.860	0.029	0.865	0.943	0.883	0.823	0.053	0.855	0.916	0.908	0.848	0.043	0.873	0.932
2	1	0.918	0.874	0.039	0.892	0.932	0.927	0.867	0.026	0.869	0.949	0.891	0.837	0.050	0.866	0.923	0.908	0.847	0.044	0.872	0.932
2	2	0.918	0.874	0.039	0.889	0.933	0.925	0.866	0.028	0.870	0.947	0.882	0.820	0.056	0.853	0.912	0.903	0.839	0.046	0.866	0.928

by comparing the linear model 2.1 with 2.2, we find that removing the PE does not affect the performance. And for the PTRE-based version, the models 3.2 and 3.4 without the PE achieve a slight performance improvement over the models 3.1 and 3.3. These experiments indicate that the explicit PE can be safely removed when the features are extracted by the CNN. Moreover, since the PE fixes the sequence length, the model without it can handle variable-length sequences more flexibly.

b) Region-wise or Position-wise?: The utilization of the local context is one of the key factors for the success of convolution in 2D vision tasks. Although the transformer can facilitate the propagation of global information, it does not pay enough attention to the local region, which may lead to important local details being overlooked. To alleviate this problem, we introduce locality to assist the attention operations. Specifically, the 3×3 convolution is used to replace the original linear projection layer, and the CFFN (Sec. III-C0c) is used to replace the original position-wise FFN. The experimental results in Tab. II reflect that the region-wise operations at different locations affect the overall performance and the FFN is more suitable to be enhanced than the projection layer by using these operations. We finally choose an optimal combination of “No. 3.4” for other experiments. Interestingly, in Tab. II, “No. 3.4” outperforms “No. 3.2” on NLPR, SIP, and STERE, but the performance on NJUD of the two is the same. This may be because most of salient objects in NJUD dataset have not complex local details, which makes the effects of local operation in the CFFN be not obvious.

c) Effectiveness of the CMIU.: In order to explore the effects of CMIU, we gradually replace the CMIU in the original TransCMD with the commonly used “Convolution-BN-ReLU” structure in the order from shallow to deep. The experimental results are listed in Tab. V. It can be seen from the table that with the gradual application of CMIU from shallow to deep, the performance of the model has been consistently improved on multiple datasets.

d) Number of SA Blocks.: The number of the intra-modal self-attention blocks (i.e. N_{im}) and the number of the cross-scale self-attention blocks (i.e. N_{cs}) are also important hyper-

parameters that directly affect the capacity of the model, and we also show a careful ablation analysis in Tab. VI for different combinations of them. The results in the table reflect that, as the number of blocks grows, the performance is no longer improved and reaches its best at $N_{im} = 2$ and $N_{cs} = 1$. This also implies that for our model, stacking more self-attention blocks does not necessarily improve performance, that is, performance is not simply positively correlated with model capacity.

e) Position of Patch-wise Embedding.: In this work, the PTRE is designed to reduce the complexity of the attention operation for high-resolution and multi-scale features, which makes our attention block have a different structure from those existing vision transformer methods [19], [20]. In addition, from Tab. II, we can see that, for our pure linear model, the introduction of PTRE also improves the accuracy of the method compared to the version with PVT-style patch-wise embedding.

f) Patch Size of the PTRE.: The size of the patch embedding in the PTRE is an important parameter. We compare three choices in Tab. IV. From the specific metrics in the table, we can see that with the increase of patchsize, the performance has changed. Compared with 4×4 and 8×8 , 16×16 has a slight decrease, especially in some metrics (S_m , F_β^ω and F_β^{adp}) of NLPR, SIP and STERE. In our opinion, the performance degradation here is due to the sequence being too short. It should be also noted that since the input image of our method is 256×256 , the resolution of the highest feature is 16×16 after being downsampled 16 times by the VGG backbone. When the patch size is 16×16 , the size of the attention map corresponding to the feature map is 1×1 , and the process of gathering information from the value is then simplified to scale the value using a specific scalar factor. Too large a window would result in too short a sequence length, which would weaken the transformer’s ability to model global interactions. The sequence lengths corresponding to these patchsizes have a small difference, which reduces the range of performance changes, for example, the length difference of the top sequences of 8×8 and 16×16 is 3. The performance of the current model itself is already high, this can be seen from the comparison of existing methods based on VGG-16 and without additional loss

TABLE VII
EFFECT OF THE HYBRID LOSS.

MODELS	NJUD					NLPR					SIP					STERE				
	S_m	F_{β}^{ω}	MAE	F_{β}^{adp}	E_m^{adp}	S_m	F_{β}^{ω}	MAE	F_{β}^{adp}	E_m^{adp}	S_m	F_{β}^{ω}	MAE	F_{β}^{adp}	E_m^{adp}	S_m	F_{β}^{ω}	MAE	F_{β}^{adp}	E_m^{adp}
UCNet [50] [†]	0.897	0.868	0.043	0.889	0.934	0.920	0.878	0.025	0.890	0.955	0.875	0.836	0.051	0.868	0.918	0.903	0.867	0.039	0.885	0.942
HDFNet [35] [‡]	0.908	0.877	0.038	0.889	0.932	0.923	0.882	0.023	0.889	0.957	0.886	0.848	0.047	0.875	0.924	0.900	0.853	0.041	0.867	0.931
Ours [†]	0.918	0.874	0.039	0.892	0.932	0.927	0.867	0.026	0.869	0.949	0.891	0.837	0.050	0.866	0.923	0.908	0.847	0.044	0.872	0.932
Ours [†] +HybridLoss	0.914	0.884	0.036	0.899	0.940	0.921	0.878	0.028	0.880	0.949	0.879	0.836	0.052	0.862	0.915	0.900	0.854	0.044	0.874	0.933
Ours [‡]	0.925	0.883	0.034	0.898	0.941	0.924	0.867	0.030	0.869	0.947	0.901	0.858	0.043	0.885	0.935	0.912	0.854	0.041	0.876	0.937
Ours [‡] +HybridLoss	0.924	0.903	0.031	0.915	0.951	0.925	0.890	0.027	0.894	0.958	0.898	0.878	0.040	0.902	0.939	0.912	0.875	0.035	0.889	0.945

functions, such as ICNet, D3Net and S2MA. These may cause the overall performance of the model to appear less sensitive to different patchsizes. Finally, in order to better adapt to the ResNet-50 model with a downsampling rate of 32 at the same time (the downsampling rate of the VGG-16 mode without the final pooling layer used in the ablation experiment is 16), we uniformly set the patchsize of the PTRE to 4×4 in other experiments.

g) *Hybrid Loss.*: During the training phase, we use only binary cross entropy loss (BCE) and the specific mathematical form is as follows:

$$L = \frac{1}{H \times W} \sum_h \sum_w -\mathcal{G}_{h,w} \log \mathcal{P}_{h,w} - (1 - \mathcal{G}_{h,w}) \log(1 - \mathcal{P}_{h,w}), \quad (4)$$

where $\mathcal{G}_{h,w}$ and $\mathcal{P}_{h,w}$ denote the value at position (h, w) on the ground truth \mathcal{G} and prediction \mathcal{P} , respectively. Since BCE only focuses on the pixel-level error and ignores the overall region constraint, some recent SOD works [13], [14], [17], [35], [50], [73], [74] additionally introduce the auxiliary region-level constraint to construct the hybrid loss, which has achieved significant results. The main focus of this paper is to improve the structural design for RGB-D SOD, therefore, the overall experiment is still based on BCE only. Therefore, we keep the structure as simple as possible and do not apply some of the existing complex modules and loss functions. The most experiments are still based on BCE only. However, to facilitate a full and detailed comparison with existing methods, we re-train our VGG-based and ResNet-based models with the hybrid loss used in [13], [50] and list results in Tab. VII. And we additionally add the results on the dataset RGBD135. Although it may cause a slight decrease in S_m , on the other metrics and most datasets, the hybrid loss can significantly improve performance and have an overall positive gain.

h) *Visualization of Attention Maps.*: To visualize the impact of attention operations at different positions, we show in Fig. 7 the learned alignment score map, i.e., the attention map, which is calculated by the dot product between the patch-wise query token corresponding to the red marker in RGB and depth images and the global key token sequence. Some interesting points are shown in these results. From “*_SA_0” to “*_SA_1”, the semantic discriminability of the features themselves is enhanced, and the scores on the related token positions are boosted, that is, the model focuses more on specific locations. From “*_SA_1” to “*_CA”, it is obvious that an information interaction between RGB and depth is carried out. From “*_CA” to “RGBD_SA”, due to the integration of

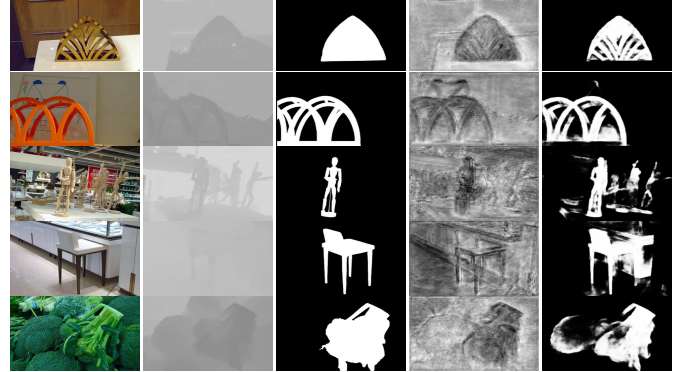


Fig. 8. Visualization of some typical failure cases. From left to right in the figure are I_{rgb} , I_d , \mathcal{G} , f_{rgb}^1 and \mathcal{P} .

features with stronger semantic information from the previous layer, the foreground token of the query pays more attention to those tokens from the saliency region. From the results in the 2nd, 3rd and 4th rows of Fig. 7, the highlighting of salient objects in the attention map of the background token also demonstrates that the attention operation does not focus only on those semantically relevant regions, but also cues that help determine their own attributes, including irrelevant regions with the reference value (i.e., saliency regions in this case).

i) *Layer Normalization or Batch Normalization?*: In the original transformer [18] and recent vision transformer methods [19], [20], [56], the authors usually choose the layer normalization [70] to normalize the tokens sequence. However, when used with convolution, batch normalization [71] may be a more efficient choice because it can be fused into the preceding convolution operation to accelerate the inference time. Besides, the results in Tab. III show the performance difference between LN and BN is not significant. So, for our models in other experiments, BN is the default choice.

j) *Some Typical Failure Cases.*: We show some typical failure cases in Fig. 8. In the first and second cases, the objects with similar structure types yet require different coverage types for prediction. Specifically, in \mathcal{G} , the gap inside the salient object is completely covered in the first sample, but not in the second. Such data may interfere with the learning process of the model. Besides, in the second case, there are some artifacts with a similar color to the foreground in the gaps of the foreground object in I_{rgb} , which interferes with the prediction of the model. And, the model has more difficulty in predicting the narrow foreground region at the edge of the image, which can also be seen in its feature map, where the lowermost part of the object region is significantly different from the rest. The

foreground and interfering objects in the latter three samples are extremely similar in appearance. It is very difficult for the model to accurately capture the object and exclude the background interference in this case. Moreover, the depth maps of these samples either have a relatively clear outline of the foreground object and the interference objects (e.g., Row 3 and 5), or the foreground object is directly blended with the background objects (e.g., Row 4). These depth maps do not provide enough valid information, and even the depth contour of the background objects brings interference to the prediction. This makes the separation of foreground and background in the prediction more complicated and directly leads to significant misclassification. In fact, all the above problems can be attributed to the ambiguity caused by low-quality depth data. To solve these problems, we need to further improve the model's ability to tolerate inaccurate depth information and adapt to low-quality data and make the model able to discover more essential differences between samples. These will be the focus of future research.

V. CONCLUSION

In this paper, we rethink the architecture design for the RGB-D SOD task. A novel transformer-based top-down information propagation path is proposed to enhance the capability of perceiving and excavating the important global cues in intra-modal features and simplify the cross-modal long-range interaction and alignment. And by using the PTRE, the computational and storage intensity of the matrix operation in the attention block is effectively reduced, which makes it possible to process multi-scale high-resolution features. In addition, the convolutional FFN further enhances the critical local details in the feature map. We also verify that the position encoding can be safely removed from the hybrid structure, which makes our model more flexible. Extensive experimental comparisons demonstrate the effectiveness of the proposed method.

REFERENCES

- [1] Y. Wei, X. Liang, Y. Chen, X. Shen, M.-M. Cheng, J. Feng, Y. Zhao, and S. Yan, "Stc: A simple to complex framework for weakly-supervised semantic segmentation," *IEEE Transactions on Pattern Analysis and Machine Intelligence*, vol. 39, no. 11, pp. 2314–2320, 2017.
- [2] X. Zhao, L. Zhang, and H. Lu, "Automatic polyp segmentation via multi-scale subtraction network," in *International Conference on Medical Image Computing and Computer-Assisted Intervention*, M. de Bruijne, P. C. Cattin, S. Cotin, N. Padoy, S. Speidel, Y. Zheng, and C. Essert, Eds. Cham: Springer International Publishing, 2021, pp. 120–130.
- [3] D.-P. Fan, G.-P. Ji, T. Zhou, G. Chen, H. Fu, J. Shen, and L. Shao, "Pranet: Parallel reverse attention network for polyp segmentation," in *International Conference on Medical Image Computing and Computer-Assisted Intervention*, 2020, pp. 263–273.
- [4] X. Lu, W. Wang, J. Shen, D. Crandall, and J. Luo, "Zero-shot video object segmentation with co-attention siamese networks," *IEEE Transactions on Pattern Analysis and Machine Intelligence*, pp. 1–1, 2020.
- [5] D.-P. Fan, W. Wang, M.-M. Cheng, and J. Shen, "Shifting more attention to video salient object detection," in *Proceedings of IEEE Conference on Computer Vision and Pattern Recognition*, 2019, pp. 8546–8556.
- [6] X. Zhao, Y. Pang, J. Yang, L. Zhang, and H. Lu, "Multi-source fusion and automatic predictor selection for zero-shot video object segmentation," in *Proceedings of the 29th ACM International Conference on Multimedia*, ser. MM '21. New York, NY, USA: Proceedings of the ACM International Conference on Multimedia, 2021, p. 2645–2653. [Online]. Available: <https://doi.org/10.1145/3474085.3475192>
- [7] R. Zhao, W. Ouyang, and X. Wang, "Unsupervised salience learning for person re-identification," in *Proceedings of IEEE Conference on Computer Vision and Pattern Recognition*, 2013, pp. 3586–3593.
- [8] V. Mahadevan and N. Vasconcelos, "Saliency-based discriminant tracking," in *Proceedings of IEEE Conference on Computer Vision and Pattern Recognition*, 2009, pp. 1007–1013.
- [9] S. Hong, T. You, S. Kwak, and B. Han, "Online tracking by learning discriminative saliency map with convolutional neural network," in *International Conference on Machine Learning*, ser. Proceedings of Machine Learning Research, F. Bach and D. Blei, Eds., vol. 37. Lille, France: PMLR, 07–09 Jul 2015, pp. 597–606. [Online]. Available: <http://proceedings.mlr.press/v37/hong15.html>
- [10] Z. Ren, S. Gao, L.-T. Chia, and I. W.-H. Tsang, "Region-based saliency detection and its application in object recognition," *IEEE Transactions on Circuits and Systems for Video Technology*, vol. 24, no. 5, pp. 769–779, 2014.
- [11] W. Wang, J. Shen, and H. Ling, "A deep network solution for attention and aesthetics aware photo cropping," *IEEE Transactions on Pattern Analysis and Machine Intelligence*, vol. 41, no. 7, pp. 1531–1544, 2019.
- [12] C. Guo and L. Zhang, "A novel multiresolution spatiotemporal saliency detection model and its applications in image and video compression," *IEEE Transactions on Image Processing*, vol. 19, no. 1, pp. 185–198, 2010.
- [13] J. Wei, S. Wang, and Q. Huang, "F³net: Fusion, feedback and focus for salient object detection," in *AAAI Conference on Artificial Intelligence*, 2020, pp. 12 321–12 328.
- [14] J. Wei, S. Wang, Z. Wu, C. Su, Q. Huang, and Q. Tian, "Label decoupling framework for salient object detection," in *Proceedings of IEEE Conference on Computer Vision and Pattern Recognition*, 2020, pp. 13 022–13 031.
- [15] X. Zhao, Y. Pang, L. Zhang, H. Lu, and L. Zhang, "Suppress and balance: A simple gated network for salient object detection," in *Proceedings of European Conference on Computer Vision*, 2020, pp. 35–51.
- [16] J.-J. Liu, Q. Hou, and M.-M. Cheng, "Dynamic feature integration for simultaneous detection of salient object, edge and skeleton," *IEEE Transactions on Image Processing*, pp. 1–15, 2020.
- [17] Y. Pang, X. Zhao, L. Zhang, and H. Lu, "Multi-scale interactive network for salient object detection," in *Proceedings of IEEE Conference on Computer Vision and Pattern Recognition*, June 2020, pp. 9410–9419.
- [18] A. Vaswani, N. Shazeer, N. Parmar, J. Uszkoreit, L. Jones, A. N. Gomez, L. u. Kaiser, and I. Polosukhin, "Attention is all you need," in *Proceedings of International Conference on Neural Information Processing Systems*, I. Guyon, U. V. Luxburg, S. Bengio, H. Wallach, R. Fergus, S. Vishwanathan, and R. Garnett, Eds., vol. 30. Curran Associates, Inc., 2017. [Online]. Available: <https://proceedings.neurips.cc/paper/2017/file/3f5ee243547dee91fdb053c1c4a845aa-Paper.pdf>
- [19] A. Dosovitskiy, L. Beyer, A. Kolesnikov, D. Weissenborn, X. Zhai, T. Unterthiner, M. Dehghani, M. Minderer, G. Heigold, S. Gelly, J. Uszkoreit, and N. Houlsby, "An image is worth 16x16 words: Transformers for image recognition at scale," in *International Conference on Learning Representations*, 2021. [Online]. Available: <https://openreview.net/forum?id=YicbFdNTTy>
- [20] W. Wang, E. Xie, X. Li, D.-P. Fan, K. Song, D. Liang, T. Lu, P. Luo, and L. Shao, "Pyramid vision transformer: A versatile backbone for dense prediction without convolutions," 2021.
- [21] K. Simonyan and A. Zisserman, "Very deep convolutional networks for large-scale image recognition," *arXiv preprint arXiv:1409.1556*, 2014.
- [22] K. He, X. Zhang, S. Ren, and J. Sun, "Deep residual learning for image recognition," in *Proceedings of IEEE Conference on Computer Vision and Pattern Recognition*, 2016, pp. 770–778.
- [23] L. Itti, C. Koch, and E. Niebur, "A model of saliency-based visual attention for rapid scene analysis," *IEEE Transactions on Pattern Analysis and Machine Intelligence*, vol. 20, no. 11, pp. 1254–1259, Nov 1998.
- [24] T. Liu, Z. Yuan, J. Sun, J. Wang, N. Zheng, X. Tang, and H.-Y. Shum, "Learning to detect a salient object," *IEEE Transactions on Pattern Analysis and Machine Intelligence*, vol. 33, no. 2, pp. 353–367, Feb 2011.
- [25] R. Achanta, S. Hemami, F. Estrada, and S. Susstrunk, "Frequency-tuned salient region detection," in *Proceedings of IEEE Conference on Computer Vision and Pattern Recognition*, June 2009, pp. 1597–1604.
- [26] J. Long, E. Shelhamer, and T. Darrell, "Fully convolutional networks for semantic segmentation," in *Proceedings of IEEE Conference on Computer Vision and Pattern Recognition*, 2015, pp. 3431–3440.
- [27] O. Ronneberger, P. Fischer, and T. Brox, "U-net: Convolutional networks for biomedical image segmentation," in *International Conference on Medical Image Computing and Computer-Assisted Intervention*, 2015, pp. 234–241.
- [28] A. Borji, M.-M. Cheng, Q. Hou, H. Jiang, and J. Li, "Salient object detection: A survey," *Computational Visual Media*, vol. 5, pp. 117–150, 2014.

- [29] W. Wang, Q. Lai, H. Fu, J. Shen, H. Ling, and R. Yang, "Salient object detection in the deep learning era: An in-depth survey," *IEEE Transactions on Pattern Analysis and Machine Intelligence*, pp. 1–1, 2021.
- [30] H. Peng, B. Li, W. Xiong, W. Hu, and R. Ji, "Rgb-d salient object detection: A benchmark and algorithms," in *Proceedings of European Conference on Computer Vision*, D. Fleet, T. Pajdla, B. Schiele, and T. Tuytelaars, Eds. Cham: Springer International Publishing, 2014, pp. 92–109.
- [31] X. Zhao, L. Zhang, Y. Pang, H. Lu, and L. Zhang, "A single stream network for robust and real-time rgb-d salient object detection," in *Proceedings of European Conference on Computer Vision*, A. Vedaldi, H. Bischof, T. Brox, and J.-M. Frahm, Eds. Cham: Springer International Publishing, 2020, pp. 646–662.
- [32] D.-P. Fan, Z. Lin, Z. Zhang, M. Zhu, and M.-M. Cheng, "Rethinking rgb-d salient object detection: Models, datasets, and large-scale benchmarks," *IEEE Transactions on Neural Networks and Learning Systems*, pp. 1–1, 2020.
- [33] L. Qu, S. He, J. Zhang, J. Tian, Y. Tang, and Q. Yang, "Rgb-d salient object detection via deep fusion," *IEEE Transactions on Image Processing*, vol. 26, no. 5, pp. 2274–2285, 2017.
- [34] J. Han, H. Chen, N. Liu, C. Yan, and X. Li, "Cnns-based rgb-d saliency detection via cross-view transfer and multiview fusion," *IEEE Transactions on Cybernetics*, vol. 48, no. 11, pp. 3171–3183, 2018.
- [35] Y. Pang, L. Zhang, X. Zhao, and H. Lu, "Hierarchical dynamic filtering network for rgb-d salient object detection," in *Proceedings of European Conference on Computer Vision*, A. Vedaldi, H. Bischof, T. Brox, and J.-M. Frahm, Eds. Cham: Springer International Publishing, 2020, pp. 235–252.
- [36] H. Chen, Y. Deng, Y. Li, T.-Y. Hung, and G. Lin, "Rgb-d salient object detection via disentangled cross-modal fusion," *IEEE Transactions on Image Processing*, vol. 29, pp. 8407–8416, 2020.
- [37] N. Wang and X. Gong, "Adaptive fusion for rgb-d salient object detection," *IEEE Access*, vol. 7, pp. 55 277–55 284, 2019.
- [38] H. Chen and Y. Li, "Progressively complementarity-aware fusion network for rgb-d salient object detection," in *Proceedings of IEEE Conference on Computer Vision and Pattern Recognition*, 2018, pp. 3051–3060.
- [39] —, "Three-stream attention-aware network for rgb-d salient object detection," *IEEE Transactions on Image Processing*, vol. 28, no. 6, pp. 2825–2835, 2019.
- [40] H. Chen, Y. Li, and D. Su, "Multi-modal fusion network with multi-scale multi-path and cross-modal interactions for rgb-d salient object detection," *Pattern Recognition*, vol. 86, pp. 376–385, 2019. [Online]. Available: <https://www.sciencedirect.com/science/article/pii/S0031320318303054>
- [41] J.-X. Zhao, Y. Cao, D.-P. Fan, M.-M. Cheng, X.-Y. Li, and L. Zhang, "Contrast prior and fluid pyramid integration for rgb-d salient object detection," in *Proceedings of IEEE Conference on Computer Vision and Pattern Recognition*, 2019, pp. 3927–3936.
- [42] Y. Piao, W. Ji, J. Li, M. Zhang, and H. Lu, "Depth-induced multi-scale recurrent attention network for saliency detection," in *Proceedings of the IEEE International Conference on Computer Vision*, 2019, pp. 7253–7262.
- [43] G. Li, Z. Liu, L. Ye, Y. Wang, and H. Ling, "Cross-modal weighting network for rgb-d salient object detection," in *Proceedings of European Conference on Computer Vision*, A. Vedaldi, H. Bischof, T. Brox, and J.-M. Frahm, Eds. Cham: Springer International Publishing, 2020, pp. 665–681.
- [44] W. Ji, J. Li, M. Zhang, Y. Piao, and H. Lu, "Accurate rgb-d salient object detection via collaborative learning," in *Proceedings of European Conference on Computer Vision*, A. Vedaldi, H. Bischof, T. Brox, and J.-M. Frahm, Eds. Cham: Springer International Publishing, 2020, pp. 52–69.
- [45] N. Liu, N. Zhang, and J. Han, "Learning selective self-mutual attention for rgb-d saliency detection," in *Proceedings of IEEE Conference on Computer Vision and Pattern Recognition*, 2020, pp. 13 753–13 762.
- [46] K. Fu, D. P. Fan, G. P. Ji, and Q. Zhao, "Jl-dcf: Joint learning and densely-cooperative fusion framework for rgb-d salient object detection," in *Proceedings of IEEE Conference on Computer Vision and Pattern Recognition*, 2020, pp. 3049–3059.
- [47] X. Zhao, Y. Pang, L. Zhang, H. Lu, and X. Ruan, "Self-supervised representation learning for rgb-d salient object detection," *ArXiv*, vol. abs/2101.12482, 2021.
- [48] L.-C. Chen, G. Papandreou, I. Kokkinos, K. Murphy, and A. L. Yuille, "Deeplab: Semantic image segmentation with deep convolutional nets, atrous convolution, and fully connected crfs," *IEEE Transactions on Pattern Analysis and Machine Intelligence*, vol. 40, no. 4, pp. 834–848, 2017.
- [49] M. Yang, K. Yu, C. Zhang, Z. Li, and K. Yang, "Denseaspp for semantic segmentation in street scenes," in *Proceedings of IEEE Conference on Computer Vision and Pattern Recognition*, June 2018, pp. 3684–3692.
- [50] J. Zhang, D.-P. Fan, Y. Dai, S. Anwar, F. Sadat Saleh, T. Zhang, and N. Barnes, "Uc-net: Uncertainty inspired rgb-d saliency detection via conditional variational autoencoders," in *Proceedings of IEEE Conference on Computer Vision and Pattern Recognition*, 2020, pp. 8579–8588.
- [51] X. Shi, Z. Chen, H. Wang, D.-Y. Yeung, W.-k. Wong, and W.-c. Woo, "Convolutional lstm network: A machine learning approach for precipitation nowcasting," in *Proceedings of International Conference on Neural Information Processing Systems*, ser. NIPS'15. Cambridge, MA, USA: MIT Press, 2015, p. 802–810.
- [52] J. Hu, L. Shen, and G. Sun, "Squeeze-and-excitation networks," *Proceedings of IEEE Conference on Computer Vision and Pattern Recognition*, pp. 7132–7141, 2018.
- [53] S. Woo, J. Park, J.-Y. Lee, and I. S. Kweon, "Cbam: Convolutional block attention module," in *Proceedings of European Conference on Computer Vision*, V. Ferrari, M. Hebert, C. Sminchisescu, and Y. Weiss, Eds. Cham: Springer International Publishing, 2018, pp. 3–19.
- [54] X. Zhu, D. Cheng, Z. Zhang, S. Lin, and J. Dai, "An empirical study of spatial attention mechanisms in deep networks," in *Proceedings of the IEEE International Conference on Computer Vision*, Oct 2019, pp. 6687–6696.
- [55] X. Wang, R. Girshick, A. Gupta, and K. He, "Non-local neural networks," in *Proceedings of IEEE Conference on Computer Vision and Pattern Recognition*, 2018, pp. 7794–7803.
- [56] H. Touvron, M. Cord, M. Douze, F. Massa, A. Sablayrolles, and H. Jégou, "Training data-efficient image transformers & distillation through attention," *arXiv preprint arXiv:2012.12877*, 2020.
- [57] S. Zheng, J. Lu, H. Zhao, X. Zhu, Z. Luo, Y. Wang, Y. Fu, J. Feng, T. Xiang, P. H. Torr, and L. Zhang, "Rethinking semantic segmentation from a sequence-to-sequence perspective with transformers," in *Proceedings of IEEE Conference on Computer Vision and Pattern Recognition*, 2021.
- [58] K. He, X. Zhang, S. Ren, and J. Sun, "Identity mappings in deep residual networks," in *Proceedings of European Conference on Computer Vision*, B. Leibe, J. Matas, N. Sebe, and M. Welling, Eds. Cham: Springer International Publishing, 2016, pp. 630–645.
- [59] R. Xiong, Y. Yang, D. He, K. Zheng, S. Zheng, C. Xing, H. Zhang, Y. Lan, L. Wang, and T. Liu, "On layer normalization in the transformer architecture," in *International Conference on Machine Learning*, ser. Proceedings of Machine Learning Research, H. D. III and A. Singh, Eds., vol. 119. PMLR, 13–18 Jul 2020, pp. 10 524–10 533. [Online]. Available: <http://proceedings.mlr.press/v119/xiong20b.html>
- [60] W. Wang, J. Shen, M.-M. Cheng, and L. Shao, "An iterative and cooperative top-down and bottom-up inference network for salient object detection," in *Proceedings of IEEE Conference on Computer Vision and Pattern Recognition*, 2019, pp. 5968–5977.
- [61] R. Ju, Y. Liu, T. Ren, L. Ge, and G. Wu, "Depth-aware salient object detection using anisotropic center-surround difference," *Signal Processing: Image Communication*, vol. 38, pp. 115–126, 2015, recent Advances in Saliency Models, Applications and Evaluations. [Online]. Available: <https://www.sciencedirect.com/science/article/pii/S0923596515001058>
- [62] Y. Cheng, H. Fu, X. Wei, J. Xiao, and X. Cao, "Depth enhanced saliency detection method," in *Proceedings of the International Conference on Internet Multimedia Computing and Service*, 2014, pp. 23–27.
- [63] C. Zhu and G. Li, "A three-pathway psychobiological framework of salient object detection using stereoscopic technology," in *International Conference on Computer Vision Workshops*, 2017, pp. 3008–3014.
- [64] Y. Niu, Y. Geng, X. Li, and F. Liu, "Leveraging stereopsis for saliency analysis," in *Proceedings of IEEE Conference on Computer Vision and Pattern Recognition*, 2012, pp. 454–461.
- [65] D.-P. Fan, M.-M. Cheng, Y. Liu, T. Li, and A. Borji, "Structure-measure: A new way to evaluate foreground maps," in *Proceedings of the IEEE International Conference on Computer Vision*, 2017, pp. 4548–4557.
- [66] F. Perazzi, P. Krähenbühl, Y. Pritch, and A. Hornung, "Saliency filters: Contrast based filtering for salient region detection," in *Proceedings of IEEE Conference on Computer Vision and Pattern Recognition*, 2012, pp. 733–740.
- [67] R. Achanta, S. Hemami, F. Estrada, and S. Süsstrunk, "Frequency-tuned salient region detection," in *Proceedings of IEEE Conference on Computer Vision and Pattern Recognition*, no. CONF, 2009, pp. 1597–1604.
- [68] D.-P. Fan, C. Gong, Y. Cao, B. Ren, M.-M. Cheng, and A. Borji, "Enhanced-alignment measure for binary foreground map evaluation," in *International Joint Conference on Artificial Intelligence*, 2018, pp. 698–704.

- [69] R. Margolin, L. Zelnik-Manor, and A. Tal, “How to evaluate foreground maps?” in *Proceedings of IEEE Conference on Computer Vision and Pattern Recognition*, 2014, pp. 248–255.
- [70] L. J. Ba, J. R. Kiros, and G. E. Hinton, “Layer normalization,” *Computing Research Repository*, vol. abs/1607.06450, 2016. [Online]. Available: <http://arxiv.org/abs/1607.06450>
- [71] S. Ioffe and C. Szegedy, “Batch normalization: Accelerating deep network training by reducing internal covariate shift,” in *International Conference on Machine Learning*, ser. ICML’15. JMLR.org, 2015, p. 448–456.
- [72] M. A. Islam, S. Jia, and N. D. B. Bruce, “How much position information do convolutional neural networks encode?” *Computing Research Repository*, vol. abs/2001.08248, 2020. [Online]. Available: <https://arxiv.org/abs/2001.08248>
- [73] X. Qin, Z. Zhang, C. Huang, C. Gao, M. Dehghan, and M. Jagersand, “Basnet: Boundary-aware salient object detection,” in *Proceedings of IEEE Conference on Computer Vision and Pattern Recognition*, 2019, pp. 7479–7489.
- [74] Z. Wu, L. Su, and Q. Huang, “Stacked cross refinement network for edge-aware salient object detection,” in *Proceedings of the IEEE International Conference on Computer Vision*, 2019, pp. 7264–7273.